Temporal Evolution of Morphology, Composition, and Structure in the Formation of Colloidal High-Entropy Intermetallic Nanoparticles

Samuel S. Soliman,[1] Gaurav R. Dey,[1] Connor R. McCormick,[1] and Raymond E. Schaak[1,2,3,*]

[1] *Department of Chemistry,* [2] *Department of Chemical Engineering, and* [3] *Materials Research Institute, The Pennsylvania State University, University Park, PA 16802, United States.*

E-mail: res20@psu.edu

ABSTRACT

Morphology-controlled nanoparticles of high entropy intermetallic compounds are quickly becoming high-value targets for catalysis. Their ordered structures with multiple distinct crystallographic sites, coupled with the "cocktail effect" that emerges from randomly mixing a large number of elements, leads to catalytic active sites capable of achieving advanced catalytic functions. Despite this growing interest, little is known about the pathways by which high entropy intermetallic nanoparticles form and grow in solution. As a result, controlling their morphology remains challenging. Here, we use the high entropy intermetallic compound (Pd,Rh,Ir,Pt)Sn, which adopts a NiAs-related crystal structure, as a model system for understanding how nanoparticle morphology, composition, and structure evolve during synthesis in solution using a slow-injection reaction. By performing a time-point study, we establish the initial formation of palladium-rich cube-like Pd-Sn seeds onto which the other metals deposit over time, concomitant with continued incorporation of tin. For (Pd,Rh,Ir,Pt)Sn, growth occurs on the corners, resulting in a sample having a mixture of flower-like and cube-like morphologies. We then synthesize and characterize a library of 14 distinct intermetallic nanoparticle systems that comprise all possible binary, ternary, and quaternary constituents of (Pd,Rh,Ir,Pt)Sn. From these studies, we correlated compositions, morphologies, and growth pathways with the constituent elements and their competitive reactivities, ultimately mapping out a framework that rationalizes the key features of the high entropy (Pd,Rh,Ir,Pt)Sn intermetallic nanoparticles based on those of their simpler constituents. We then validated these design guidelines by applying them to the synthesis of a morphologically pure variant of flower-like (Pd,Rh,Ir,Pt)Sn particles, as well as a series of (Pd,Rh,Ir,Pt)Sn particles with tunable morphologies based on control of composition.

KEYWORDS

High entropy alloys, intermetallic compounds, nanoparticles, nanochemistry, reaction pathways

INTRODUCTION

Nanoparticles of high-entropy materials, such as alloys, have important physical and catalytic properties that arise from the synergistic effects of randomly mixing five or more principal elements within a crystalline lattice.[1,2] These so-called "cocktail" effects, along with high surface-to-volume ratios, position nanoparticles of high entropy materials as effective catalysts with enhanced activity and selectivity,[3,4] as well as electronic and chemical behavior that is different from their compositionally simpler counterparts.[5] Intermetallic compounds, which are alloys that have an ordered crystal structure containing multiple distinct crystallographic sites, are especially interesting catalytic materials. Their ordered crystal structures inherently create isolated active sites on the surface of the catalyst, which facilitates enhanced catalytic functions, such as different reactivities and suppression of catalyst deactivation through poisoning.[6] The formation of solid solutions on specific crystallographic sites can also lead to improved catalytic activity due to the resulting changes in the electronic properties of the metals.[7,8] Nanoparticles of high entropy intermetallic compounds are therefore expected to combine the attributes of synergistic active sites and electronic structures that arise from both the ordered crystal structures and the mixing of a large number of metals. High entropy intermetallic nanoparticle catalysts are starting to emerge, although only a few have been reported. For example, high entropy intermetallic PtRhFeNiCu nanoparticles[9] exhibited excellent catalytic performance and resistance to CO poisoning for ethanol oxidation and (PtCoCu)(GeGaSn) nanoparticles[10] have similarly been demonstrated as active and stable catalysts for propane dehydrogenation.

Synthesis is an important prerequisite to harnessing the catalytic properties of high entropy intermetallic nanoparticles for fundamental studies and applications, but capabilities remain limited. High entropy intermetallic nanoparticles are often synthesized using high temperatures and rapid quenching. For example, $(FeCoNi)_{86}$–(Al_7Ti_7) high entropy intermetallic nanocomposites[11] were synthesized using arc melting, supported (NiFeCu)–(GaGe)[12] and (PtCoCu)(GeGaSn)[10] nanoparticles were synthesized by calcination of metal-impregnated high surface area silica, and $(Pt_{0.8}Pd_{0.1}Au_{0.1})(Fe_{0.6}Co_{0.1}Ni_{0.1}Cu_{0.1}Sn_{0.1})$ high entropy intermetallic nanoparticles[13] were synthesized with Joule heating and rapid cooling. Solution-based methods that produce colloidal high entropy nanoparticles are only recently starting to emerge for alloy systems,[14–26] and much still remains to be discovered about how they form and grow. Colloidal synthesis methods are even more rare for intermetallic compounds. These methods, which have been demonstrated for PtRhBiSnSb[27] and PtBiPbNiCo,[28] generally consist of preloading metal precursor salts into a vial containing common particle-stabilizing surfactants such as oleylamine and octadecene and heating until product formation is complete. Additional surfactants and reducing agents such as cetyltrimethyl ammonium bromide (CTAB) and ascorbic acid help to direct the shape and size of intermetallic nanoparticles, which have been reported to form hexagonal plates, truncated octahedra, and pseudo-spherical particles.[29] Given the different chemical characteristics of the constituent elements, coupled with the ordered crystal structures that depend on composition and other factors, the morphologies of high entropy intermetallic nanoparticles are expected to be challenging to control. Identifying and understanding the role of reaction conditions, composition, and crystal structure in the formation and growth of high entropy intermetallic nanoparticles, as well as their simpler constituent compounds, is an important step toward being able to predict and control their morphologies.

Here, we systematically investigate the formation of a colloidal high-entropy intermetallic nanoparticle system, (Pd,Rh,Ir,Pt)Sn, to elucidate and understand how composition influences

morphology. We chose (Pd,Rh,Ir,Pt)Sn because it is considered to be a high entropy phase based on convention in the field and its constituent binary *M*Sn (*M* = Pd, Rh, Ir, Pt) intermetallic compounds adopt NiAs and NiAs-related crystal structures.[28,30-32] Using a slow-injection method, we synthesized colloidal nanoparticles of (Pd,Rh,Ir,Pt)Sn along with all possible combinations of its constituent binary, ternary, and quaternary intermetallics using identical protocols. Through these comprehensive synthetic studies of this library of 14 distinct nanoparticle systems, we were able to deduce how composition and the competitive reactivities of the metal reagents influenced the morphological characteristics and the growth pathways. We uncovered important relationships between key aspects of the simpler intermetallics that translate to their high entropy analogues, providing a framework for predicting and controlling the morphological features of colloidal high entropy intermetallic nanoparticles. We then validated this pathway by applying it to the rational synthesis of a morphologically-pure variant of (Pd,Rh,Ir,Pt)Sn and other metal-rich variants of (Pd,Rh,Ir,Pt)Sn where composition defines morphology. This knowledge is useful for designing high entropy intermetallic nanoparticles containing targeted compositions and morphologies by judiciously choosing the constituent elements, without modifying other reaction parameters or incorporating different surface stabilizing species.

RESULTS AND DISCUSSION

Synthesis and Characterization of (Pd,Rh,Ir,Pt)Sn

In the synthesis of metallic nanoparticles, one of the most common methods involves thermal decomposition of metal salts using oleylamine as both a reducing agent and a surfactant.[33,34] Throughout the literature, these metal salts can be introduced to the solvent initially before heating or injected, slowly or rapidly, into the already-heated solvent. We chose to start from this existing approach, tailoring our protocols to allow for the synthesis of single-phase and compositionally complex intermetallic and high entropy intermetallic nanoparticles. We converged on a slow injection rate of 0.25 mL/min, which favors mixing of the constituent metals in the intermetallic nanoparticles rather than forming phase-segregated nanoparticles of the individual metals.

We chose (Pd,Rh,Ir,Pt)Sn as our model system to investigate how composition influences morphology. Colloidal nanoparticles of PdRhIrPtSn were previously found to form a disordered alloy when an equimolar ratio of all five metals, *i.e.*, 1:1:1:1:1 Pd:Rh:Ir:Pt:Sn, was used in a similar synthetic protocol [14]. Here, to favor the formation of the *M*Sn intermetallic compound, we used a 1:1 ratio of the total transition metals to tin, *i.e.*, 0.25:0.25:0.25:0.25:1 Pd:Rh:Ir:Pt:Sn. Figure 1 shows characterization data for the (Pd,Rh,Ir,Pt)Sn nanoparticles formed from a slow injection of 4 mL of metal reagent solution (containing the aforementioned ratios of metal salts) at 0.25 mL/min into heated oleylamine and octadecene at 315 °C, followed by cooling ambiently to 230 °C, then quenching in a room-temperature water bath. Figure 1a shows a HAADF-STEM image of the (Pd,Rh,Ir,Pt)Sn nanoparticle product, which contains two distinct subpopulations. Enlarged HAADF-STEM images of the regions indicated by the dashed boxes are also shown. One subpopulation (yellow box) consists of particles with a flower-like morphology that have average diameters of approx. 50–70 nm. These nanoflowers appear to have sheet-like protrusions that emanate from a central core. This morphology is frequently observed for colloidal nanoparticles of layered materials, such as transition metal chalcogenides[35] and layered oxides[36] and hydroxides,[37] but is much less common for the metals, alloys, and intermetallics that are related to (Pd,Rh,Ir,Pt)Sn. The other subpopulation (cyan box) contains smaller particles having average diameters of 20–30 nm. The morphologies of these particles appear to be derivatives of cubes and elongated cubes, with additional growth at the corners.

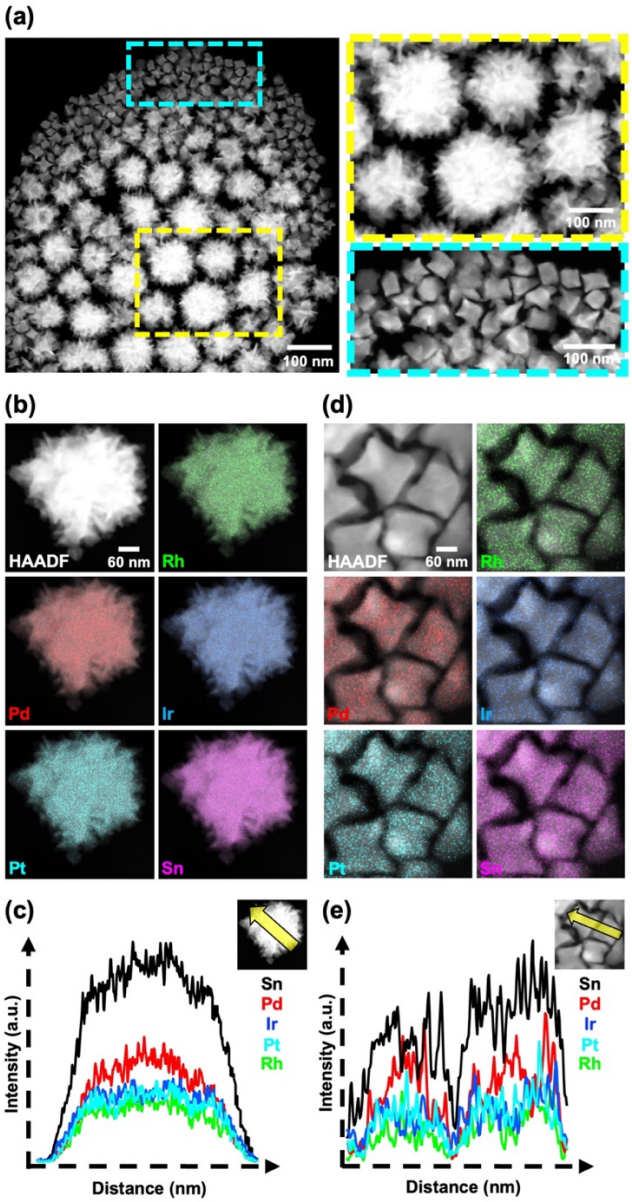

Figure 1. (a) HAADF-STEM image of an as-synthesized sample of (Pd,Rh,Ir,Pt)Sn nanoparticles. Enlarged regions of the two subpopulations, larger flower-like particles and smaller cube-like particles, are shown in the yellow and cyan dashed boxes, respectively. HAADF-STEM images and corresponding overlaid STEM-EDS element maps for Pd, Pt, Rh, Ir, and Sn are shown for single particles of the (b) flower-like and (d) cube-like (Pd,Rh,Ir,Pt)Sn nanoparticles. The corresponding STEM-EDS line scans are shown in (c) and (e), respectively. The yellow arrow highlights the regions included in the line scans and the corresponding intensity profiles for Sn (black), Pd (red), Ir (blue), Pt (cyan), and Rh (green) are shown.

HAADF-STEM images and corresponding STEM-EDS element maps and line scans of Pd, Rh, Ir, Pt, and Sn for representative particles from each subpopulation are shown in Figures 1b-e. The data in Figures 1b and 1d confirm that all five elements are colocalized and uniformly distributed throughout both the larger flower-like particles and the smaller cube-like particles. The average composition of both subpopulations of particles, as determined by analysis of the STEM-EDS data, is $Pd_{0.38}Rh_{0.26}Ir_{0.21}Pt_{0.28}Sn$ (normalized to Sn). This composition corresponds to an

overall stoichiometry of $M_{1.13}$Sn, which is slightly metal-rich, but close to the 1:1 *M*:Sn ratio of reagents that is loaded in the reaction flask. (Additional characterization data, including larger-area images, ensemble EDS spectra, and SAED patterns for each subpopulation, are included in Figure S1 of the Supporting Information.) The accompanying STEM-EDS line scans in Figure 1c and 1e provide additional insights into how the elements are distributed throughout each subpopulation of particles. The line scan for the flower-like particles (Figure 1c) shows that the elements fully colocalize across the protrusions and valleys, with no evidence of segregation. In contrast, the line scan for the cube-like particles (Figure 1e) shows spikes of Pd that are anti-correlated with the other elements, providing evidence of Pd-rich regions with all elements colocalized elsewhere.

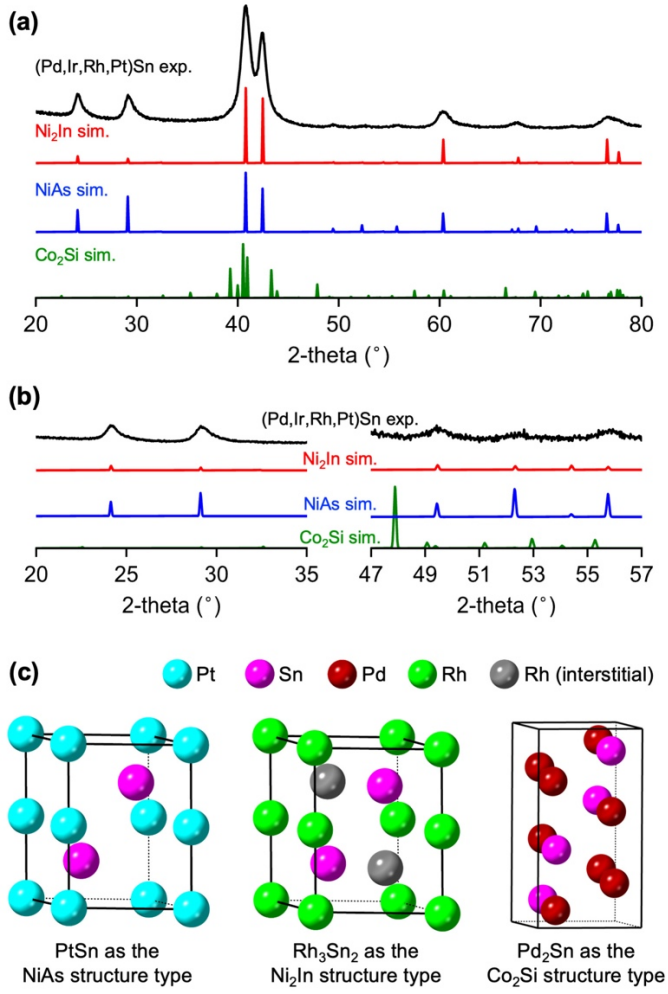

Figure 2. (a) Experimental XRD data (black) for the as-synthesized (Pd,Ir,Rh,Pt)Sn nanoparticles, along with simulated XRD patterns for (Pd,Ir,Rh,Pt)Sn in the NiAs, Ni_2In, and Co_2Si structure types. (Details are included in the Supporting Information.) (b) Enlarged regions, including both the experimental and simulated patterns. (c) The crystal structures of PtSn (NiAs structure), Rh_3Sn_2 (Ni_2In structure with half-filled Rh sites), and Pd_2Sn (Co_2Si structure), as described in the text.

The powder XRD pattern for the (Pd,Rh,Ir,Pt)Sn nanoparticles is presented in Figure 2a, along with expanded regions in Figure 2b to highlight the weak-intensity reflections. However, before analyzing the powder XRD data, it is helpful to consider the NiAs and NiAs-related phases that

exist in the constituent binary intermetallic systems, *i.e.*, Pd-Sn, Rh-Sn, Ir-Sn, and Pt-Sn. Figure 2c shows the crystal structure of NiAs, which is adopted by PtSn and IrSn. The NiAs structure consists of a hexagonally close packed (hcp) array of Sn atoms with all octahedral holes occupied by the transition metal. Figure 2c also shows the crystal structure of Ni_2In, which is a metal-rich variant of NiAs. Ni_2In, which is adopted by binary Rh-Sn and Pd-Sn intermetallics, consists of the NiAs crystal structure with the addition of a transition metal in the bipyramidal interstitial sites. These sites can be filled between occupancies of 0 and 1. For the binary Rh-Sn and Pd-Sn intermetallics, the occupancy of this interstitial site is 0.5, which results in a stoichiometry of $M_{1.5}Sn$, or M_3Sn_2; the corresponding intermetallics are therefore Rh_3Sn_2 and Pd_3Sn_2. Co_2Si, which can also be adopted by Pd-Sn, is also shown in Figure 2c.[38] Relative to NiAs and Ni_2In, the crystal structure of Co_2Si is different and it has an orthorhombic (rather than hexagonal) unit cell. These structural similarities and differences are important to understand, given the elements that are incorporated into the (Pd,Rh,Ir,Pt)Sn high entropy intermetallic and how their XRD patterns are related.

Along with the experimental XRD pattern for the high entropy intermetallic nanoparticles in Figure 2a, simulated XRD patterns for (Pd,Rh,Ir,Pt)Sn in the NiAs, Ni_2In, and Co_2Si structures are shown for comparison. (The simulated patterns assume equal occupancy of all metal sites with 25% each of Pd, Rh, Ir, and Pt.) Subtle, but important, differences in the XRD patterns and the number and relative intensities of the peaks can be observed. Due to the similarities between NiAs and Ni_2In, including their similarly sized hexagonal unit cells, most of the characteristic reflections are identical between the two structures, including the two highest-intensity reflections. However, due to the partial filling of the bipyramidal interstitial sites, certain reflections disappear and the relative intensities of many of the reflections change. The largest difference is the much lower intensities of the two lowest-angle peaks relative to the highest-intensity peaks in Ni_2In whereas in NiAs, the two lowest-angle peaks are quite intense relative to the highest-intensity reflections. Due to the larger orthorhombic unit cell of the Pd_2Sn structure relative to NiAs and Ni_2In, there are more reflections, many of which are located around the two highest-intensity reflections. All three crystal structures are distinguishable by careful analysis of the powder XRD data.

Given these considerations, the experimental XRD pattern appears to match best with a simulated pattern based on a hexagonal Ni_2In crystal structure having lattice parameters of a = 4.26 Å and c = 5.51 Å. We ruled out NiAs because the intensities of the lowest-angle reflections relative to the highest-intensity reflections, as well as the low relative intensities of the peaks between 49 and 57 º2θ, differ from what is predicted based on the NiAs structure. Given the *hkl* values for the peaks that have different relative intensities, preferred orientation is unlikely to be responsible. By EDS, we also observe a metal-rich composition, and by XRD, we observe lattice parameters that are larger than the range expected for NiAs-type compounds; both the composition and expanded unit cell (due to additional filled interstitial sites) are therefore more consistent with Ni_2In than with NiAs. Accordingly, we classify the high entropy intermetallic as having an overall formula of $(Pd,Rh,Ir,Pt)_3Sn_2$ corresponding to a partially filled Ni_2In structure, although for simplicity, we will keep referring to it as (Pd,Rh,Ir,Pt)Sn.

Time Point Study of (Pd,Rh,Ir,Pt)Sn Formation

To understand how the (Pd,Rh,Ir,Pt)Sn nanoparticles formed, we carried out a time point study by rapidly quenching reactions prior to completion and analyzing them to determine the compositional, structural, and morphological evolution of the particles throughout the reaction, especially given the observation of Pd-rich cores in the smaller cube-like subpopulation of

particles in Figure 1. It is known in the literature that colloidal intermetallic nanoparticles often form by first generating seed particles *in situ*, followed by diffusion of reactive metal species into the seeds.[39-41] As an example, PtSn nanoparticles made using a similar colloidal method with oleylamine as the capping ligand and reducing agent did not form through simultaneous co-reduction of platinum and tin salts, but rather by the initial formation of platinum seeds due to its more noble character, followed by reduction and diffusion of tin into the platinum seeds.[42,43]

Recall that the reaction to form (Pd,Rh,Ir,Pt)Sn involves slowly injecting 4 mL of a precursor solution having a 0.25:0.25:0.25:0.25:1 molar ratio of Pd:Rh:Ir:Pt:Sn into oleylamine and octadecene at 315 °C. We were able to obtain a sample at an early time point of 30 seconds after the start of the injection by rapid quenching. HAADF-STEM and STEM-EDS data for a representative particle from among those that were most frequently observed in the 30-second sample are shown in Figure 3a; additional data are shown in Figure S2. These images indicate a cube-like morphology with growth at the corners, similar to the morphology of the smaller subpopulation observed in Figure 1. As confirmed by the STEM-EDS element maps, the corresponding EDS line scan, and the histogram showing the average composition for a larger ensemble of particles, all five elements are present with an overall composition of $Pd_{0.29}Rh_{0.21}Ir_{0.05}Pt_{0.14}Sn_{0.31}$. However, the amounts of Pd and Sn are significantly larger than those of Rh and Pt, and only a small amount of Ir is present. The STEM-EDS element maps and line scan in Figure 3a both suggest that the center of these cube-like particles contains mostly Pd and the growths at the corners consist of mostly Ir, Rh, Pt, and Sn, which are colocalized in those regions. Figure 3a also includes a plot showing the radial profile of the corresponding SAED pattern, which was taken on a wider region of the sample. (SAED was used instead of XRD because the amount of sample isolated from the earliest time points was insufficient for bulk analysis; the radial profile of the SAED pattern is closely related to an XRD pattern and can be used for similar purposes. The x-axis was converted to 2-theta for direct comparison with the XRD data, as described in the Experimental Section.) The SAED pattern and corresponding radial profile match a face centered cubic (fcc) structure. Taken together, the observations in Figure 3a suggest that at the earliest stages of the reaction, the particles that form first are nominally cube-shaped with predominantly Pd at the core and deposition of Rh, Ir, Pt, and Sn at the corners are the majority product. Some particles that are observed in the 30-second time point sample (Figure S2) have more tin throughout, suggesting that the reaction progresses quickly to incorporate increasing amounts of Sn.

By two minutes (Figure 3b), the morphology and composition continue to evolve through continued growth on the Pd-rich seeds and further incorporation of all elements. The HAADF-STEM image in Figure 3b, as well as the images in Figure S3, show additional growth of the protrusions on the corners of the particles. The corresponding STEM-EDS element maps and line scan show that the Pd-rich core remains, although more Sn is incorporating into it. The corner growths contain all five elements, which suggests that the high entropy (Pd,Rh,Ir,Pt)Sn phase deposits directly on the Pd-rich core. The average composition of the sample isolated at two minutes, based on EDS analysis, is $Pd_{0.19}Rh_{0.15}Ir_{0.11}Pt_{0.17}Sn_{0.38}$, which represents an increase in the amounts of Ir, Pt, and Sn relative to the 30-second sample and is consistent with the continued reduction and diffusion of tin into the nanoparticles throughout the duration of the slow injection process. Analysis of the SAED data confirms the persistence of the fcc alloy phase observed in Figure 3a, along with the emergence of a NiAs intermetallic phase. The observed behavior in this sample, relative to the prior one, is consistent with previous studies on the conversion of fcc metal seed nanoparticles, such as Pt, into a NiAs-type PtSn intermetallic upon Sn diffusion and

incorporation. Here, continued growth of the (Pd,Rh,Ir,Pt)Sn intermetallic occurs concomitantly with further diffusion of Sn into the nanoparticles, including into the core region.

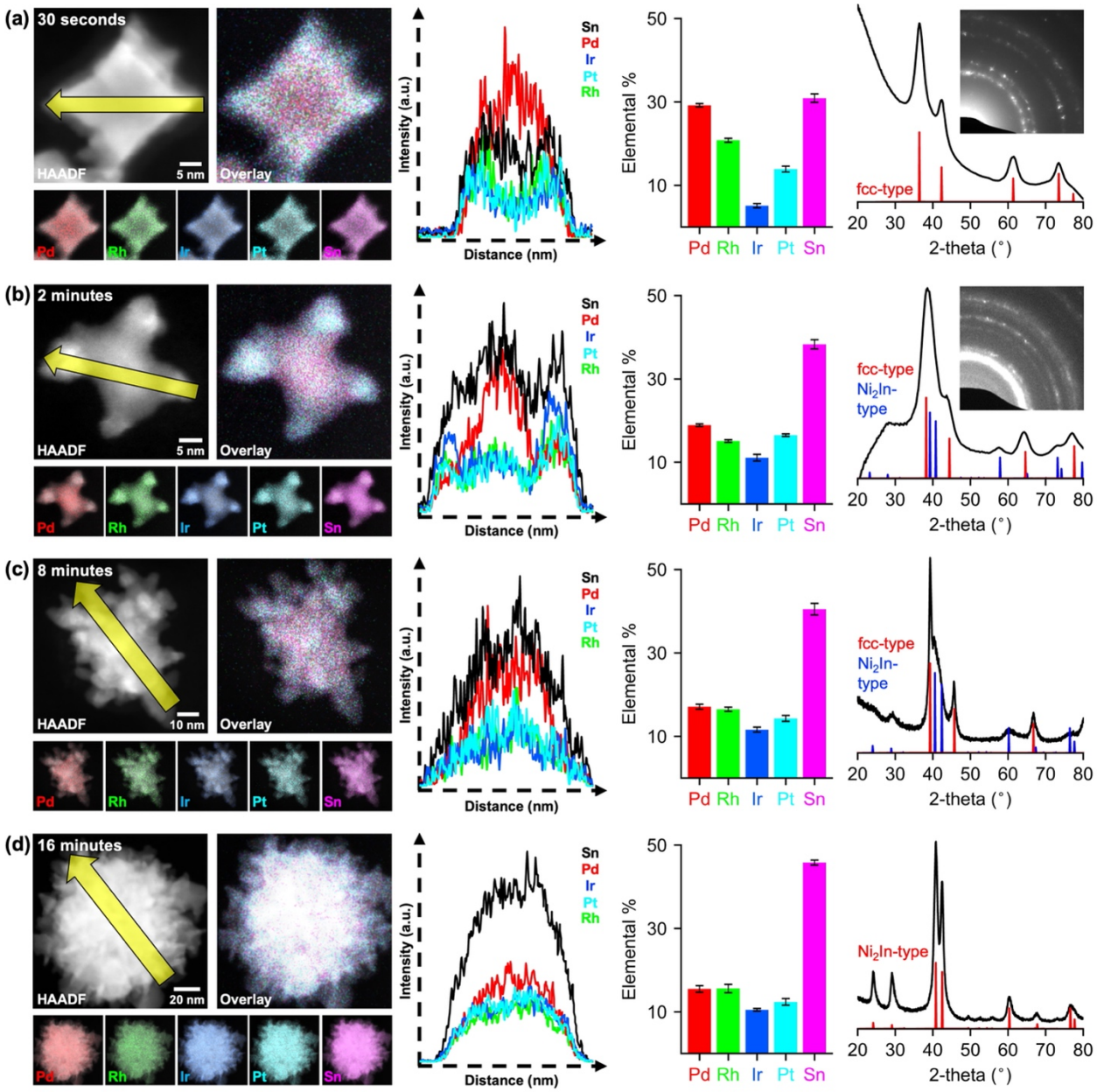

Figure 3. Characterization data for samples isolated after (a) 30 seconds, (b) 2 minutes, (c) 8 minutes, and (d) 16 minutes during the synthesis of (Pt,Rh,Ir,Pt)Sn nanoparticles. For each sample, the data shown includes a representative HAADF-STEM image with corresponding overlaid STEM-EDS element maps for Pd, Rh, Ir, Pt, and Sn, as well as an overlay of all elements; a line scan across the particle, as indicated by the yellow arrow; a histogram (based on analysis of the ensemble EDS data in Figures S2–S5 in the Supporting Information) showing the average percentages of each element; and diffraction data. Experimental powder XRD data is shown in (c) and (d). The amount of sample isolated in the 30-second and 2-minute time points was insufficient for XRD, so in (a) and (b) the corresponding SAED pattern is shown, along with a radial profile translated to a form that is comparable to the XRD data, as described in the Experimental Section. Simulated XRD patterns for the majority and minority phases are shown in red and blue, respectively.

The HAADF-STEM image in Figure 3c indicates that the morphology at 8 minutes is similar to that at 2 minutes, with more pronounced growth of protrusions outward from the core and the onset of the flower-like morphology that was observed in Figure 1a; additional images are shown in Figure S4. The corresponding STEM-EDS element maps and line scan show significant co-localization of Pd and Sn in similar ratios, with smaller amounts of Rh, Ir, and Pt that are also co-localized. The composition, based on EDS analysis, was $Pd_{0.17}Rh_{0.17}Ir_{0.12}Pt_{0.14}Sn_{0.40}$, which is largely unchanged from the previous time point. While composition is not changing significantly from 2 to 8 minutes, the amount of time spent at 315 °C facilitates diffusion and crystallization of the NiAs-related phase. The experimental powder XRD pattern confirms that there is still a significant population of fcc particles along with an increase in the relative amount of the NiAs-related intermetallic phase. However, the broadness of the NiAs-related peaks indicates that the grain sizes remain small, which is consistent with the hypothesis that the NiAs-related (Pd,Rh,Ir,Pt)Sn intermetallic is seeded by the Pd-rich surface.

By 16 minutes, the data in Figures 3d and S5 indicate that the reaction has reached completion, based on comparison to the data in Figure 1. The HAADF-STEM image shows the fully-formed nanoflower morphology of the (Pd,Rh,Ir,Pt)Sn particles, which appear by XRD as a single Ni_2In phase. The STEM-EDS element maps show homogeneous distribution of all five elements, and the corresponding line scan confirms the co-localization. There is no longer evidence for significant amounts of isolated Pd by XRD or STEM-EDS, indicating that Sn has diffused into the core of the particle and largely transformed the Pd seeds, along with the entire particle, to (Pd,Rh,Ir,Pt)Sn. (There is slightly higher Pd signal in the center of the nanoflowers, suggesting that a small amount of the Pd-rich core may remain, but its colocalization with Rh, Ir, Pt, and Sn suggest that it does not comprise a significant amount of the overall particle.) The flower-like particle has a composition of $Pd_{0.16}Rh_{0.16}Ir_{0.11}Pt_{0.12}Sn_{0.46}$, or $Pd_{0.35}Rh_{0.35}Ir_{0.24}Pt_{0.26}Sn$ normalized to Sn, which corresponds to an overall *M*:Sn stoichiometry of $M_{1.2}Sn$ that is close to the stoichiometry in Figure 1.

Together, the data in Figure 3 suggest that the (Pd,Rh,Ir,Pt)Sn intermetallic nanoparticles begin as fcc Pd-rich Pd-Sn cube-like seeds with some Rh and Pt, and a smaller amount of Ir, incorporated toward the corners. Over time, Rh, Ir, Pt, and Sn continue to incorporate, predominantly through growth of a NiAs/Ni_2In-related phase at the corners, with all elements appearing to deposit together. Eventually, Sn incorporates and diffuses throughout the particles, including the Pd-rich core, resulting in an overall uniform composition of (Pd,Rh,Ir,Pt)Sn in a nanoflower morphology. This proposed pathway is consistent with both the TEM and XRD data, which show the morphological evolution expected as well as a gradual decrease in the fcc component and an increase in the NiAs/Ni_2In components, eventually converging on Ni_2In as more metals are incorporated. The HRTEM images in Figure S6 are also consistent with this proposed pathway. Based on analysis of the lattice fringes, the nanoflowers in Figure S6 appear polycrystalline with the protrusions consisting of individual crystallites growing outward from the core, which resembles the seed particles isolated at the earliest time point (Figure 3a). The cubes are similarly polycrystalline (Figure S6), with the deposits on the corners being crystallographically distinct from the Pd-rich core.

Binary M-Sn Intermetallic Nanoparticles

Given the morphological and compositional evolution observed in Figure 3, along with the compositional complexity of the (Pd,Rh,Ir,Pt)Sn system and the range of compositions and crystal structures that the constituent binary intermetallics could adopt based on their phase diagrams,

we decided next to study constituent binary, ternary, and quaternary *M*-Sn intermetallics made using the same synthetic protocol as the high entropy system. We wanted to identify the compositions, crystal structures, and morphologies of these constituent intermetallics toward the goal of understanding how these features evolved and to eventually map out correlations that help to rationalize the observed morphologies of the high entropy intermetallic nanoparticles. We therefore synthesized and characterized the constituent binary intermetallic compounds in the Pd-Sn, Rh-Sn, Ir-Sn, and Pt-Sn systems. These experiments were carried out using the same synthetic protocol where 2 mL of the transition metal precursor solutions and 2 mL of the tin precursor solutions were mixed, degassed, and slowly injected into a flask containing oleylamine and octadecene at 315 °C. Figure 4 shows HAADF-STEM images and experimental powder XRD patterns for each of the products.

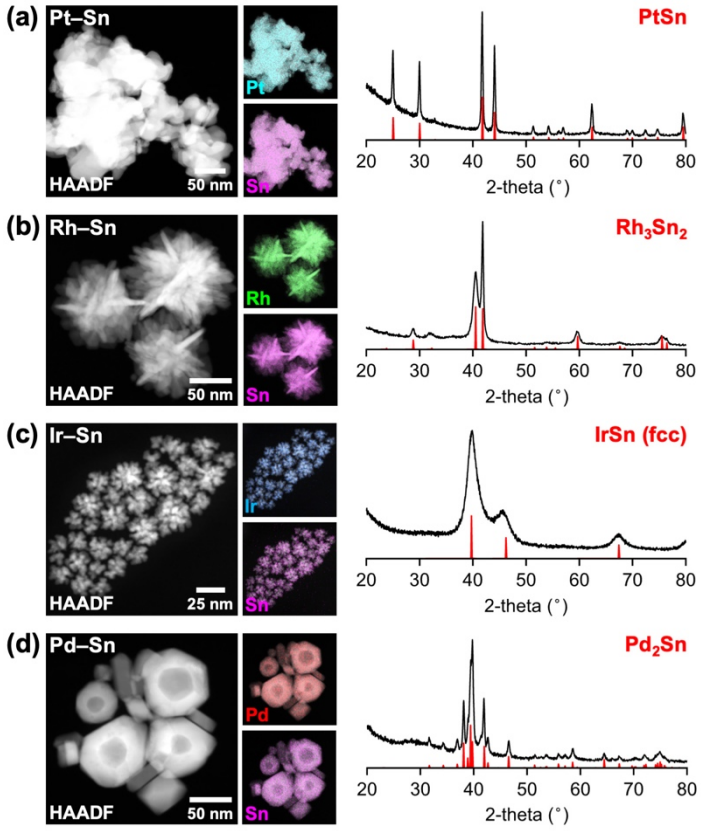

Figure 4. Characterization data for binary intermetallics: (a) Pt–Sn, (b) Rh–Sn, (c) Ir–Sn, and (d) Pd–Sn. For each sample, a HAADF-STEM image and corresponding overlaid STEM-EDS element maps for the constituent elements are shown, along with experimental (black) and simulated (red) XRD patterns.

For Pt-Sn, the XRD pattern in Figure 4a confirms the formation of NiAs-type PtSn. The HAADF-STEM image shows that the particles are polydisperse with an irregular morphology and the XRD peaks are somewhat sharp, which is consistent with the large grain sizes observed by TEM. The composition determined by STEM-EDS analysis was $Pt_{0.45}Sn_{0.55}$, which is close to the expected 1:1 Pt:Sn ratio (Figure S7). The HAADF-STEM image and powder XRD data for Rh-Sn in Figure 4b show the formation of Ni_2In-type Rh_3Sn_2 nanoparticles with EDS analysis indicating a metal-rich composition of $Rh_{0.55}Sn_{0.45}$ (Figure S8). Interestingly, the morphology of the Rh_3Sn_2 nanoparticles is reminiscent of that of the high entropy (Pd,Rh,Ir,Pt)Sn nanoparticles with spiky protrusions. The powder XRD pattern indicates that the peak near 41.8 º2θ is narrower than the

peak to its left, as was also the case for the (Pd,Rh,Ir,Pt)Sn particles in Figure 2a. This observation indicates that the particles are thicker along the $(2\bar{1}0)$ plane, which is parallel to the z-axis of Ni_2In and bisects the Sn and bipyramidal metal sites, and therefore consistent with the sheet-like nature of the protrusions on the flower-like particles.

Figure 4c shows that Ir-Sn forms as a face-centered cubic alloy with a composition of $Ir_{0.54}Sn_{0.46}$ (Figure S9). The IrSn nanoparticles consist of agglomerates of small 5–10 nm crystallites, which are reminiscent of the morphology observed in the growing high entropy (Pd,Rh,Ir,Pt)Sn intermetallic at the 8-minute time point observed in Figure 3c. Pd-Sn (Figure 4d) forms as Co_2Si-type Pd_2Sn. EDS analysis indicates a composition of $Pd_{0.64}Sn_{0.36}$ (Figure S10), which matches well with that of Pd_2Sn but is significantly different than the Pd:Sn stoichiometry that was injected. The Pd_2Sn nanoparticles consist of a polydisperse mixture of elongated cubes with faceted tips, along with much larger hexagonal particles having hollow centers. The apparent holes in the centers of the larger hexagonal particles are consistent with Kirkendall voids that are known to form in Sn-based intermetallic systems due to an imbalance in diffusion rates of outgoing *vs* incoming species.[44] We hypothesize here that Pd forms first, then Sn diffuses in to form the Pd_2Sn product, based on the knowledge that palladium salts reduce relatively rapidly in oleylamine but tin salts cannot be reduced by oleylamine unless accompanied by another metal that helps to autocatalyze its reduction.[14]

The observations in Figure 4 correlate well with key aspects of the time-point studies in Figure 3 and help us begin to understand the evolution of composition, structure, and morphology during the formation of the (Pd,Rh,Ir,Pt)Sn high entropy intermetallic nanoparticles. The seeds that form initially during the time study in Figure 3a contain mostly Pd and Sn and their morphology consists of elongated cubes that are reminiscent of the smaller subpopulation of Pd_2Sn particles in Figure 4d, which also consist of elongated cubes. As more Rh, Ir, and Pt are incorporated in the time point study, the key morphological characteristics of the binary intermetallic particles begin appearing in the growing (Pd,Rh,Ir,Pt)Sn particles: Rh_3Sn_2 forms spiky protrusions, IrSn forms more dendritic nanostructures, and PtSn is polydisperse with evidence of underlying facets. Morphological aspects of the (Pd,Rh,Ir,Pt)Sn particles, and how they evolve over time, can therefore be correlated with their constituent binary intermetallics.

Ternary M_1-M_2-Sn Intermetallic Nanoparticles

Using the same protocol, we next synthesized and characterized all six possible ternary intermetallic compositions (Rh-Pt-Sn, Ir-Pt-Sn, Pd-Pt-Sn, Rh-Pd-Sn, Ir-Pd-Sn, Ir-Rh-Sn) to understand how the addition of a second transition metal influences the crystallographic and morphological outcome (Figure 5a-f). We began by investigating Rh-Pd-Sn for two reasons. First, in the earliest stages of (Pd,Rh,Ir,Pt)Sn high entropy intermetallic nanoparticle formation, the primary elements were Pd and Sn with some Rh (Figure 3a). Second, Rh-Sn and Pd-Sn both have a stable Ni_2In phase but formed different binary intermetallics (Ni_2In-type Rh_3Sn_2 and Co_2Si-type Pd_2Sn) (Figure 4). Figure 5a shows the HAADF-STEM image, overlaid STEM-EDS element maps, and experimental powder XRD pattern for the Rh-Pd-Sn product isolated from a reaction with nominal 0.5:0.5:1 ratios of Rh:Pd:Sn. The morphology, which appears as octahedra, elongated octahedra, and other hexagonally and multi-faceted particles having an average diameter of approx. 15 nm, is distinctly different from its constituent binary intermetallics as well as the (Pd,Rh,Ir,Pt)Sn high entropy intermetallic. All the elements are colocalized and uniformly distributed throughout the particles. Analysis of the EDS data (Figure S11) indicates a composition of $Rh_{0.26}Pd_{0.30}Sn_{0.44}$, which corresponds to $Rh_{0.59}Pd_{0.68}Sn$ (normalized to Sn) with an

overall metal-rich $M_{1.27}Sn$ stoichiometry that is expected for partially-filled Ni_2In. The XRD pattern is consistent with Ni_2In-type (Rh,Pd)Sn and the lattice constants of a = 4.34 Å and c = 5.59 Å are close to those predicted by Vegard's law (a = 4.36 Å, c = 5.61 Å) based on the experimentally determined composition. A peak in the XRD pattern at 38.4 °2θ corresponds to a minor Pd_2Sn phase, which is consistent with the slower reduction of rhodium salts compared to palladium salts and allows the early formation of the binary Pd-Sn intermetallic that competes with the formation of the ternary Rh-Pd-Sn phase.

For the Ir-Pd-Sn system, shown in Figures 5b and S12, the overall morphology is similar to Rh-Pd-Sn with largely octahedral-shaped and multi-faceted particles, along with additional deposits that decorate the surface. The powder XRD pattern is consistent with a Ni_2In-type phase (a = 4.31 Å, c = 5.57 Å), as was the case for Rh-Pd-Sn, with a slight decrease in both lattice constants relative to Rh-Pd-Sn. Additionally, the peak at 39.7 °2θ matches that of fcc IrSn, which is the phase observed in Figure 4c for the binary Ir-Sn nanoparticles. The HAADF-STEM element map in Figure 5b shows that the deposits on the surface contain Sn and are rich in Ir but deficient in Pd, and also that the larger particles to which the deposits are attached contain primarily Pd and Sn. Analyzing one of the deposits (Figure 5g) revealed a composition of $Ir_{0.43}Pd_{0.21}Sn_{0.36}$, confirming that the deposits are mostly IrSn. Similarly, analyzing the center of the larger particles (Figure 5g) revealed a composition of $Ir_{0.17}Pd_{0.43}Sn_{0.39}$, which is heavily Pd-rich. It is therefore likely that the deposits observed by HAADF-STEM correspond to the fcc IrSn phase observed by XRD; at this point the IrSn deposits have not yet combined, through diffusion and crystallization, with the Pd-Sn seeds, and remain as separate phases. The relative ratios of Pd and Ir to Sn are much greater here than in the five-element system, which correlates with the relative rates of reduction of the corresponding metal salts. Lower solubility of Ir in Pd may also play a role, but overall, these results are consistent with previous reports indicating a preference of Ir to form as small crystallites using similar reaction conditions.[45] Consistent with this hypothesis, we observe visually that Ir metal and Ir-Sn intermetallics take longer to form than Pd and Pd-Sn. We therefore rationalize the composition and morphology of the Ir-Pd-Sn system as resulting from the rapid formation of Pd-rich Pd-Sn seeds followed by the deposition of IrSn.

At this point in our study, our hypothesis is that Pd-rich seeds form first and then the additional metal incorporates through diffusion and/or deposition. We therefore next considered the Pt-Pd-Sn system (Figure 5c), based on the visual observation that both Pd and Pt reagents appear to reduce instantaneously upon injection of the metal reagents into the heated solvent while those of Ir and Rh do not. The morphology of Pt-Pd-Sn is similar to that of both binary intermetallics, PtSn and Pd_2Sn, with large and polydisperse particles that are multi-faceted. XRD data indicates a NiAs phase with a = 4.08 Å and c = 5.48 Å, which is consistent with the composition of $Pd_{0.26}Pt_{0.21}Sn_{0.53}$ ($Pd_{0.49}Pt_{0.40}Sn$ normalized to Sn) determined by EDS analysis (Figure S13). Weaker-intensity peaks in the XRD pattern correspond to the most intense reflections expected for fcc Pt and Pd, which is attributed to the rapid reduction rates of the platinum and palladium salts under these conditions (Figure S14), and therefore competition with formation of the M-Sn intermetallics. Rh-Pt-Sn (Figure 6d) is similar to Pt-Pd-Sn, with a polydisperse and multi-faceted morphology and lattice parameters (a = 4.03 A, c = 5.53 Å) and composition ($Rh_{0.23}Pt_{0.24}Sn_{0.53}$, or $Rh_{0.43}Pt_{0.45}Sn$ normalized to Sn) that are consistent with NiAs (Figure S15). The powder XRD data also indicate the presence of minor amounts of the fcc phases Pt_3Sn and Rh.

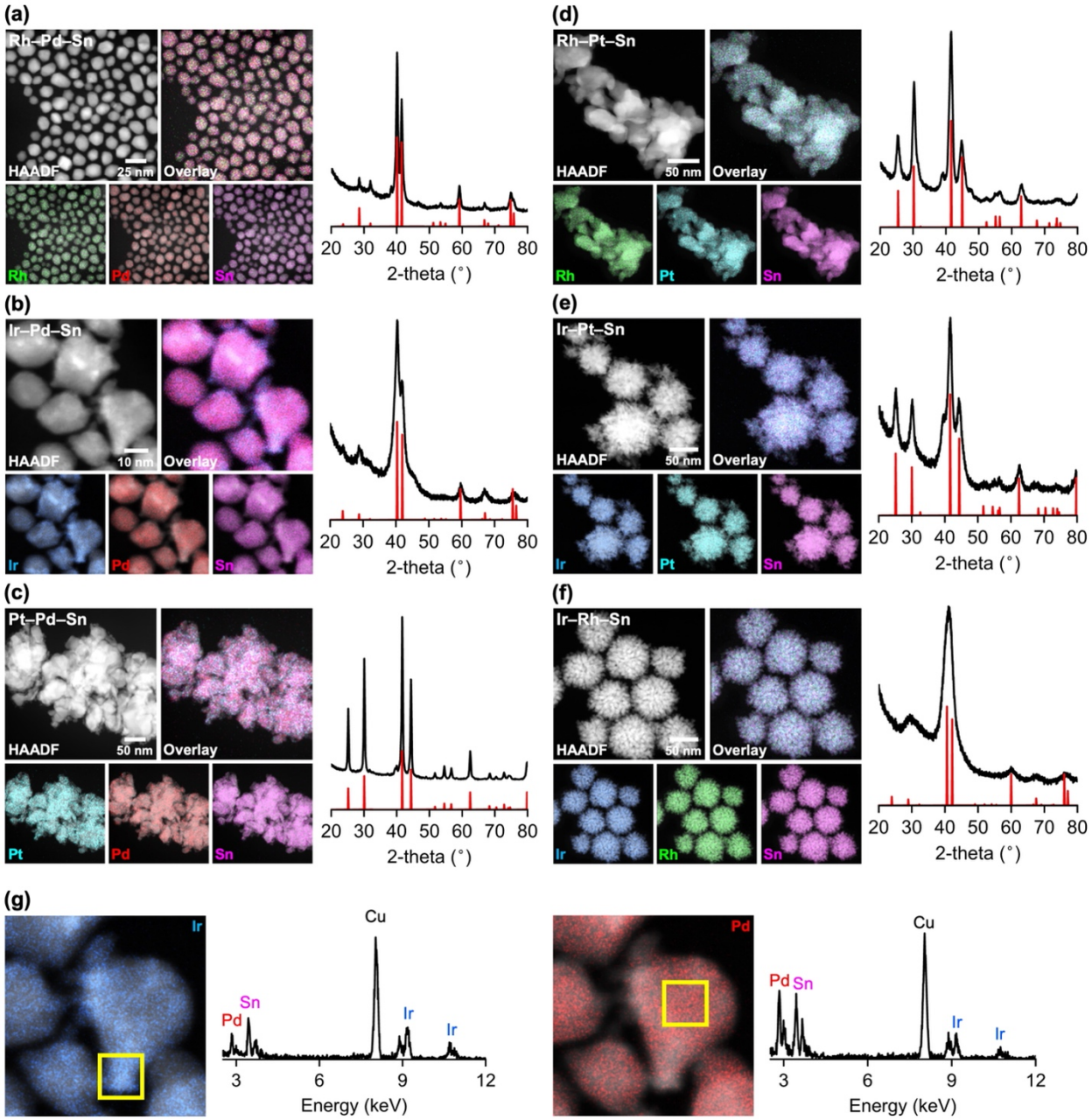

Figure 5. Characterization data for the ternary intermetallics: (a) Rh–Pd–Sn (Ni_2In), (b) Ir–Pd–Sn (Ni_2In), (c) Pt–Pd–Sn (NiAs), (d) Rh–Pt–Sn (NiAs), (e) Ir–Pt–Sn (NiAs), and (f) Ir–Rh–Sn (Ni_2In). For each sample, a HAADF-STEM image and corresponding overlaid STEM-EDS element maps for the constituent elements are shown, as well as an overlay of all elements. Experimental (black) and simulated (red) XRD patterns are also shown. Enlarged regions of the STEM-EDS element maps for Ir and Pd from the Ir–Pd–Sn sample in (b) are shown in (g), along with EDS spectra collected from the regions indicated by the yellow boxes.

We now move to the remaining Ir-containing systems, Ir-Pt-Sn (Figure 5e) and Ir-Rh-Sn (Figure 5f). Both show similar nanoflower morphologies that are polydisperse and spherical with protrusions that grow outward from a central core. Additionally, both are reminiscent of the binary IrSn intermetallic and the (Pd,Rh,Ir,Pt)Sn high entropy intermetallic, and STEM-EDS element maps confirm colocalization of all three elements throughout both types of particles. However,

their XRD patterns are distinct. For Ir-Pt-Sn, EDS analysis (Figure S16) indicates a composition of $Ir_{0.23}Pt_{0.26}Sn_{0.51}$ ($Ir_{0.45}Pt_{0.51}Sn$ normalized to Sn), and XRD indicates a NiAs crystal structure with a = 4.08 Å and c = 5.50 Å, along with fcc Pt as a minor phase, which correlates with the rapid reduction of platinum salts relative to those of iridium, as mentioned earlier. However, given the slower reduction of the platinum salt versus the palladium salt, we do not observe the apparent multi-step seeded growth, having distinct elements occupying the core and the surface deposits, that was observed in the Ir-Pd-Sn system. For Ir-Rh-Sn, the composition by EDS (Figure S17) is $Ir_{0.25}Rh_{0.29}Sn_{0.46}$ ($Ir_{0.54}Rh_{0.63}Sn$) and XRD indicates a Ni_2In crystal structure with a = 4.28 Å and c = 5.54 Å, which is consistent with the metal-rich composition. There are no observable minor phases in the Ir-Rh-Sn sample, which is consistent with the slower reduction of both Ir and Rh salts. For many of the platinum-containing intermetallics, including Pt-Sn and Pd-Pt-Sn, we observe irregular and dendritic morphologies, which are commonly seen in Pt nanoparticle systems.[46] Given the reduction rate of the rhodium salt, which is faster than that of the iridium salt (Figure S14), as well as the tendency of iridium to form small nanocrystalline deposits, one would predict Rh-Pt-Sn to form with an irregular dendritic morphology, and this indeed is the morphology that is observed.

Comparison and analysis of the HAADF-STEM, STEM-EDS, and XRD data for the six ternary intermetallics add to the insights gained from the binary systems and help us to further understand how composition, structure, and morphology evolve during formation of the (Pd,Rh,Ir,Pt)Sn high entropy intermetallic nanoparticles. Specifically, the ternary systems allow us to competitively analyze combinations of different elements to help validate hypotheses about the rates at which the various metals reduce and incorporate. For the three ternary systems that contain Pd and Sn, the particles are generally small (< 20 nm) and faceted. Those that contain Ir have dendritic protrusions with evidence of deposition on the surfaces of compositionally distinct seeds. This observation suggests that the metals that reduce the fastest, Pd and Pt, form seeds with Sn, and then Ir incorporates through deposition with other metals. Together, these ternary systems provide insights into how the compositions and morphologies evolve, and our observations are consistent with those of both the time-point study and the final (Pd,Rh,Ir,Pt)Sn product.

Quaternary M_1–M_2–M_3–Sn Intermetallic Nanoparticles

Building on the binary intermetallics in Figure 4 and the ternary intermetallics in Figure 5, we also synthesized and characterized the four quaternary systems (Ir-Rh-Pt-Sn, Ir-Rh-Pd-Sn, Ir-Pd-Pt-Sn, Rh-Pd-Pt-Sn) that are components of the (Pd,Rh,Ir,Pt)Sn high entropy intermetallic (Figure 6). We began with Rh-Pd-Pt-Sn, as it did not contain Ir, which at this point in the study we hypothesize is a key driver of the spiky protrusions. The morphology of the Rh-Pd-Pt-Sn particles, shown in Figure 6a, consists of a mixture of highly faceted particles that are reminiscent of binary Pd-Sn and Pt-Sn and ternary Rh-Pd-Sn and Pd-Pt-Sn, and all elements are homogeneously distributed throughout the particles. These binary and ternary intermetallics spanned the NiAs, Ni_2In, and Co_2Si structure types, but for Rh-Pd-Pt-Sn, we observe a Ni_2In phase with a composition determined by EDS analysis (Figure S18) of $Rh_{0.17}Pd_{0.21}Pt_{0.16}Sn_{0.46}$, or $Rh_{0.37}Pd_{0.45}Pt_{0.35}Sn$ normalized to Sn. This behavior is expected as Pd-Sn and Rh-Sn are both able to adopt the Ni_2In-phase. As in the high entropy (Pd,Rh,Ir,Pt)Sn phase, there is more Pd than Rh and Pt, which is consistent with the fast reduction kinetics of Pd, the formation of Pd-rich seeds, and concomitant reduction and diffusion of Rh, Pt, and Sn.

Next, we chose Ir-Pd-Pt-Sn to directly compare and contrast with Rh-Pd-Pt-Sn. Interestingly, the morphology of Ir-Pd-Pt-Sn is comparable to that of Rh-Pd-Pt-Sn, with a variety of faceted particles

(Figure 6b). All elements appear to be co-localized, with some evidence of the surface deposits that were previously observed for the Ir-containing systems. The overall composition based on EDS analysis (Figure S19) is $Ir_{0.13}Pd_{0.17}Pt_{0.16}Sn_{0.53}$ ($Ir_{0.25}Pd_{0.32}Pt_{0.30}Sn$ normalized to Sn), and XRD confirms a NiAs structure due to the increase of Sn incorporation as well as the large increase in the relative intensities of the two lowest-angle reflections compared to the two most intense reflections. Analysis of one of the small growths that appears in the HAADF-STEM image as a high-contrast region yields a composition of $Ir_{0.31}Pd_{0.12}Pt_{0.15}Sn_{0.42}$, which is rich in Ir (relative to Pd and Pt) and therefore confirms that this is an Ir-rich deposit (Figure S19). Based on these observations, we hypothesize that Pd-rich seeds form first in both Ir-Pd-Pt-Sn and Rh-Pd-Pt-Sn but the Rh and Pt salts co-reduce and incorporate together while Ir salts will both co-reduce and incorporate with the other metals while also depositing. This process slightly alters the morphology of the final quaternary intermetallic nanoparticles, making Ir-Pd-Pt-Sn subtly different than Rh-Pd-Pt-Sn.

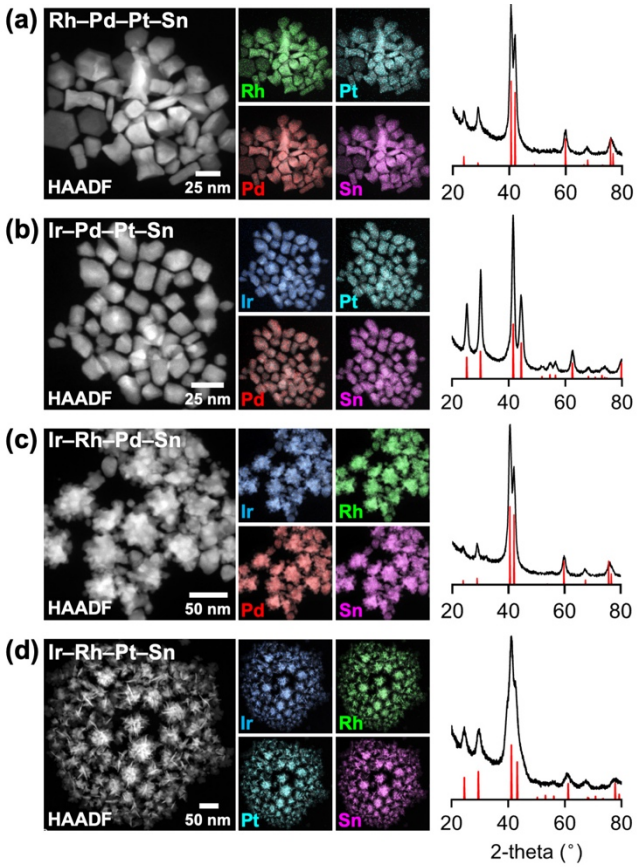

Figure 6. Characterization data for the quaternary intermetallic: (a) Rh–Pd–Pt–Sn (Ni_2In), (b) Ir–Pd–Pt–Sn (NiAs), (c) Ir–Rh–Pd–Sn (Ni_2In), and (d) Ir–Rh–Pt–Sn (NiAs). For each sample, a HAADF-STEM image and corresponding overlaid STEM-EDS element maps for the constituent elements are shown, along with experimental (black) and simulated (red) XRD patterns.

We were then interested in the Ir-Rh-Pd-Sn system, as it includes both of the slower-reducing metals (Ir, Rh) along with the rapidly-reducing Pd. Figure 6c shows a morphology that is most similar to the early time points (Figure 3b, 3c), as well as binary Ir-Sn and ternary Ir-Pd-Sn. All elements appear to be colocalized, although some regions have a higher amount of Ir, relative to the other transition metals, towards the edges of the particles, which suggests the Ir-rich surface

deposits. EDS analysis (Figure S20) indicates an average composition of $Ir_{0.15}Rh_{0.20}Pd_{0.22}Sn_{0.43}$ ($Ir_{0.35}Rh_{0.47}Pd_{0.51}Sn$ normalized to Sn), while a region corresponding to a presumed Ir-rich deposit has a composition of $Ir_{0.24}Rh_{0.19}Pd_{0.13}Sn_{0.43}$. These compositions confirm Ir-rich deposits on a Pd-rich core. XRD indicates that Ir-Rh-Pd-Sn crystallizes as a Ni_2In phase, which is consistent with the metal-rich composition.

Finally, Ir-Rh-Pt-Sn contains no Pd, and therefore is incapable of forming a Pd-rich core. Interestingly, the morphology is much closer to that of the high entropy (Pd,Rh,Ir,Pt)Sn nanoparticles (Figure 6d). The key morphological difference between Ir-Rh-Pd-Sn and Ir-Rh-Pt-Sn is that instead of Ir-rich deposits in Ir-Rh-Pd-Sn, there are sheet-like protrusions in Ir-Rh-Pt-Sn that are reminiscent of the sheets that protrude outward from the central core in (Pd,Rh,Ir,Pt)Sn. The morphology is also related to that of binary Rh-Sn. For the Pd-containing systems, we noted the growth and diffusion of Ir, Pt, and some Rh initiating at the corners of the Pd-rich seed. In this case, without Pd, this similar growth is most likely occurring on Pt-rich seeds that form rapidly upon injection of the precursor solution, as the other two metal reagents (Ir, Rh) reduce comparatively slowly. The composition based on EDS analysis (Figure S21), $Ir_{0.14}Rh_{0.19}Pt_{0.15}Sn_{0.52}$ ($Ir_{0.27}Rh_{0.37}Pt_{0.29}Sn$ normalized to Sn), is Rh-rich, which is consistent with Rh-rich sheets depositing. STEM-EDS and XRD analyses indicate that Ir-Rh-Pt-Sn forms a NiAs-type phase due to the increased amount of Sn that is incorporated as well as the differences in the relative intensities of the peaks, as discussed for the Ir-Pd-Pt-Sn system above.

The quaternary systems provide additional insights into the interplay among the constituent elements in defining the composition, structure, and morphology of the high entropy (Pd,Rh,Ir,Pt)Sn intermetallic nanoparticles. These studies confirm that Ir is necessary for initiating seeded growth, which grows the intermetallic nanoparticles outward and also keeps the particle sizes small and, as is relevant for catalysis, the surface area high. It also confirms that the relative rates of reduction of the constituent metal salts define the composition of the core vs the deposits that grow outward from the surface.

Application of the (Pd,Rh,Ir,Pt)Sn Formation Pathway to Additional Systems

Given the insights and understanding that emerged from the time-point studies and the studies of the constituent binary, ternary, and quaternary systems above, we can target additional systems having features that can be predicted in advance and then synthesized rationally. Here, we focus on two applications to both validate and apply the proposed formation pathway: a higher-yield synthesis of a (Pd,Rh,Ir,Pt)Sn sample having one morphology (rather than the mixed-subpopulation sample in Figure 1) and (Pd,Rh,Ir,Pt)Sn samples having different morphologies.

We began by targeting a higher-yield synthesis of the flower-like (Pd,Rh,Ir,Pt)Sn nanoparticles. Our knowledge of the formation pathway indicates that a cube-like Pd-rich phase forms first, and that subsequent deposition of Ir (along with the other transition metals) leads to the protrusions that ultimately define the nanoflower morphology. We also now know that Rh uniquely defines the sheet-like nature of the protrusions that were part of the flower-like particles in Figure 1, and as validated by the XRD data in Figure 2. Because of these considerations, we approached this target by modifying the composition. We made sure that all elements were still present at levels of ≥ 5%, to be consistent with conventional definitions of multiprincipal element compounds such as high entropy phases, but we decreased the amount of Pd to limit the formation of Pd-rich seeds and also decreased the amounts of Ir and Pt to allow Rh-Sn to have a primary effect on morphology. We anticipated that this change would ensure that there was not a significant amount

of Pd-rich seeds left over once surface deposition of the other metals (with tin) commenced. Finally, we increased the relative amount of Rh because it was the Rh-containing systems (RhSn, RhIrPtSn) that had the sheet-like protrusions that were characteristic of the flower-like particles in Figure 1. Accordingly Figure 7a shows a HAADF-STEM image containing mostly flower-like (Pd,Rh,Ir,Pt)Sn nanoparticles, and the accompanying STEM-EDS element maps confirms that all five elements are homogeneously distributed throughout. The composition (Figure S22), normalized to Sn, is $Pd_{0.23}Rh_{0.58}Ir_{0.13}Pt_{0.17}Sn$, which is nearly identical to the ratio of metal reagents that was injected. The powder XRD data indicates a Ni_2In phase, as was observed for RhSn, and the narrower width of the peak near 42.3 º2θ relative to that at 40.6 º2θ is consistent with the XRD data in Figure 2, which correlated to the sheet-like protrusions.

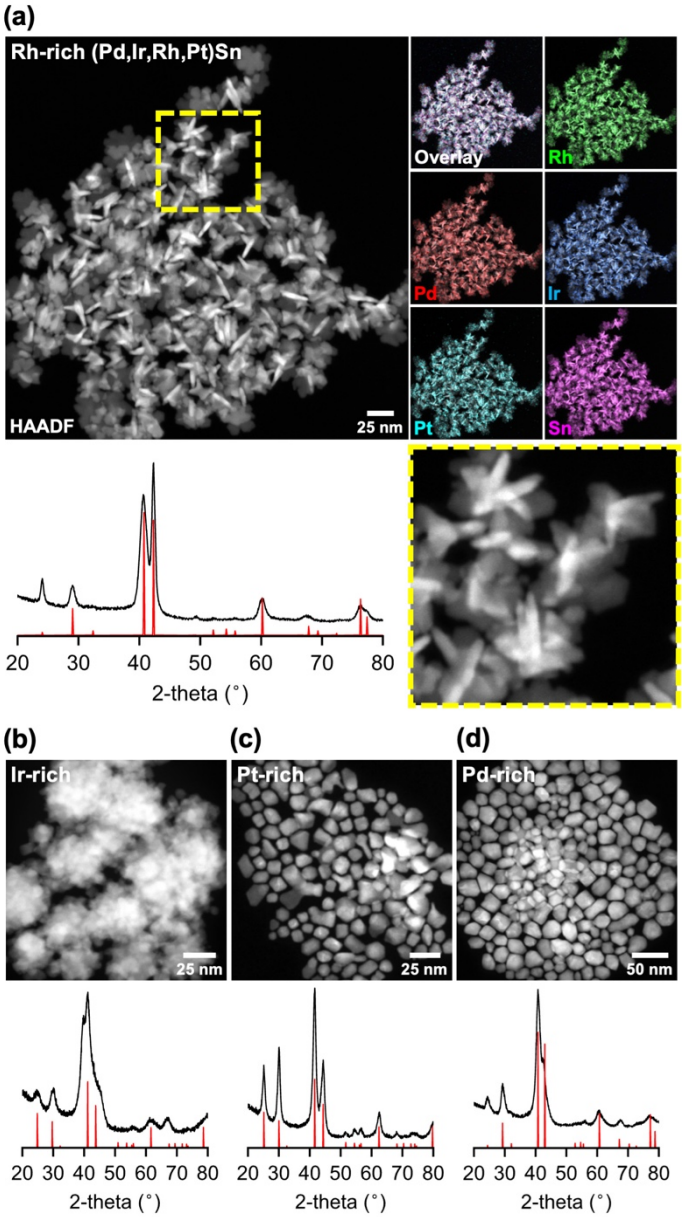

Figure 7. Characterization data for Rh-rich, Ir-rich, Pt-rich, and Pd-rich samples of (Pd,Rh,Pt,Ir)Sn nanoparticles. (a) HAADF-STEM image and corresponding overlaid STEM-EDS element maps for

Pd,Pt,Rh,Ir, and Sn, as well as an overlay of all elements. An enlarged region, as highlighted by the yellow box, is also shown. An experimental (black) and simulated (red) XRD pattern is also shown. HAADF-STEM images and corresponding experimental (black) and simulated (red) XRD patterns for (b) Ir-rich (Pd,Rh,Ir,Pt)Sn, (c) Pt-rich (Pd,Rh,Ir,Pt)Sn, and (d) Ir-rich (Pd,Rh,Ir,Pt)Sn are also shown.

The data in Figure 7a show how modifying composition modifies morphology, where the morphological features can be predicted based on previous observations of the simpler constituent intermetallics. In Figure 7b-d, we apply this rationale to other compositions and morphologies. Based on the knowledge we have gained through the preceding studies, we would predict that Ir-rich (Pd,Rh,Ir,Pt)Sn would have a flower-like morphology with discrete protrusions that grow outward from a central core, rather than the sheet-like protrusions of the Rh-rich sample. Indeed, Figure 7b confirms that $Pd_{0.20}Rh_{0.20}Ir_{0.44}Pt_{0.16}Sn$ particles have a morphology matching closely with the morphologies of IrSn, IrPdSn, and RhIrPdSn. Similarly, we would predict Pt-rich (Pd,Rh,Ir,Pt)Sn to consist of faceted particles without significant flower-like character, and that is the morphology observed for $Pd_{0.16}Rh_{0.16}Ir_{0.11}Pt_{0.38}Sn$ in Figure 7c. Finally, we would predict Pd-rich (Pd,Rh,Ir,Pt)Sn to appear very similar to the Pt-rich analogue, and Figure 7d , which shows faceted $Pd_{0.62}Rh_{0.16}Ir_{0.10}Pt_{0.14}Sn$ particles, validates that prediction. (Additional data for the nanoparticles in Figure 7 are shown in Figure S23–S25.)

CONCLUSIONS

In conclusion, we used nanoparticles of (Pd,Rh,Ir,Pt)Sn as a model high entropy intermetallic system to understand the interrelationships among composition, structure, and morphology, which all are important to control for their emerging applications in catalysis. Through time-dependent studies, we established how key features of the (Pd,Rh,Ir,Pt)Sn nanoparticles evolved during their synthesis. We further synthesized and characterized nanoparticles of the 14 constituent binary, ternary, and quaternary intermetallics of (Pd,Rh,Ir,Pt)Sn. These studies provided glimpses of the competitive reactivities of the different metal reagents under a constant set of reaction conditions, which allows us to correlate the evolution of composition and morphology with the constituent elements. These insights allowed us to rationally design syntheses to achieve higher-yield syntheses of morphologically pure (Pd,Rh,Ir,Pt)Sn nanoparticles and tune morphology by tuning composition. The key take-away lessons are that the behavior of simpler constituent intermetallics predicts the behavior of the more complex high entropy intermetallic and that the relative reduction rates of the metal salt reagents defines the order in which they incorporate, which in turn defines how their composition and morphology evolve. These design principles simplify the rational synthesis of high entropy intermetallic compounds by providing tuning knobs to control composition and morphology, which is a prerequisite for using them in application that require such features, including catalysis.

EXPERIMENTAL SECTION

Chemicals

Palladium(II) acetylacetonate [$Pd(acac)_2$, 99%], rhodium(III) acetylacetonate [$Rh(acac)_3$, 97%], tin(II) chloride [$SnCl_2$, 98%], and antimony(III) chloride [$SbCl_3$, 99%] were purchased from Sigma-Aldrich. Platinum(II) acetylacetonate [$Pt(acac)_2$, ≥48.0% Pt] and iridium(IV) chloride [$IrCl_4$, ≥56.5% Ir] were purchased from Alfa Aesar. Octadecene [ODE, 90%, technical grade] and technical grade oleylamine [tg-OLAM, 70%] were purchased from Sigma-Aldrich. Toluene and acetone were of analytical grade. All the above chemicals were used as received without further purification.

Synthesis of intermetallic nanoparticles

In a 50-mL, 3-neck round bottom flask with a reflux condenser, thermocouple, gas flow adapter, and a rubber septum, 10 mL of ODE and 6 mL of tg-OLAM were combined and heated to 110 °C under vacuum for 1 hour. The vessel was then cycled between Ar and vacuum three times, placed under Ar and slowly heated to 315 °C. Meanwhile, precursor solutions of $Pd(acac)_2$, $Rh(acac)_2$, $IrCl_4$, $Pt(acac)_2$, and $SnCl_2$ were prepared by dissolving 32.19, 41.98, 35.20, 42.27, and 19.42 mg of each respective metal salt in 10 mL of tg-OLAM. Heating and sonication were used to ensure the complete dissolution of each precursor salt. For each individual intermetallic nanoparticle synthesis, 2 mL of the $SnCl_2$ solution, and 2 mL of the appropriate transition metal reagent solution (see below) would be combined in a septum capped vial. The amounts of each element depended on the desired composition. For example, (Pd,Rh,Ir,Pt)Sn would require 500 µL of each individual transition metal solution [$Pd(acac)_2$, $Rh(acac)_2$, $IrCl_4$, $Pt(acac)_2$] and 2 mL of the $SnCl_2$ solution, whereas PtSn would require 2 mL of the $Pt(acac)_2$ solution and 2 mL of the $SnCl_2$ solution. This combined solution, having a total volume of 4 mL, was then placed under vacuum for 15 minutes. The vial was then cycled between Ar and vacuum and placed under Ar. The 4-mL precursor solution mixture was then injected slowly over 16 min at a rate of 0.25 mL/min into the solvent flask at the reaction temperature. (The 0.25 mL/min injection rate was chosen to be slower than in the synthesis of PdRhIrPtSn high entropy alloy nanoparticles[14] in order to better favor intermetallic formation by modulating the fast reduction of the palladium and platinum salts; rapid injection did not result in the formation of isolatable nanoparticles.) At the end of the reaction, the reaction flask was allowed to cool from 315 °C to 230 °C followed by a room-temperature water bath quench. The product was finally isolated by washing the particles with a 1:4 mixture of toluene and acetone followed by centrifugation and resuspension in toluene. The washing step was carried out twice and the final product was resuspended in toluene.

Characterization

A FEI Talos F2000X S/TEM operating at an accelerating voltage of 200 kV was used to collect high angle annular dark field scanning transmission electron microscopy (HAADF-STEM) images and STEM energy dispersive X-ray spectroscopy (STEM-EDS) element maps. Velox 3.6.0 software was used to interpret the STEM-EDS element map data. The EDS lines mapped were Pd Lα, Rh Lα, Ir Lα, Pt Lα, Sn Lα, and Sb Lα. EDS quantification was done using Pd Lα, Rh Lα, Ir Lα, Pt Lα, Sn Lα, and Sb Lα. A Malvern PANalytical Empyrean III using Cu Kα radiation was used to collect powder X-ray diffraction (XRD) data. All crystal structures shown were generated using CrystalMaker and all simulated diffraction patterns were generated using CrystalDiffract.[30-32,38] Both are distributed by CrystalMaker Software Ltd., Oxford, England (www.crystalmaker.com). Information about lattice parameters and crystal structure types are shown in Table S1. The SAED patterns were analyzed and converted to a radial profile using the ImageJ software. Using the d-spacings obtained from the SAED pattern, which is given in units of 1/nm, we converted the d-spacings to angstroms. We then used Braggs law to obtain values for θ, which we plotted against the intensity from the SAED patterns.

ASSOCIATED CONTENT

Supporting Information

The Supporting Information is available free of charge on the ACS Publications website.

- Additional XRD, EDS, TEM, SAED, and STEM-EDS data.

AUTHOR INFORMATION

Corresponding Author
* res20@psu.edu

Notes
The authors declare no competing financial interest.

ACKNOWLEDGMENT
This work was supported by the U.S. National Science Foundation under grant CHE-2203353. TEM and XRD data were acquired at the Materials Characterization Lab of the Penn State Materials Research Institute.

REFERENCES

(1) Yeh, J. W.; Chen, S. K.; Lin, S. J.; Gan, J. Y.; Chin, T. S.; Shun, T. T.; Tsau, C. H.; Chang, S. Y. Nanostructured High-Entropy Alloys with Multiple Principal Elements: Novel Alloy Design Concepts and Outcomes. *Adv. Eng. Mater.* **2004**, *6* (5), 299–303.

(2) Cantor, B.; Chang, I. T. H.; Knight, P.; Vincent, A. J. B. Microstructural Development in Equiatomic Multicomponent Alloys. *Mater. Sci. Eng. A* **2004**, *375–377*, 213–218.

(3) Sun, Y.; Dai, S. High-Entropy Materials for Catalysis: A New Frontier. *Sci. Adv.* **2021**, 7 (20).

(4) Xin, Y.; Li, S.; Qian, Y.; Zhu, W.; Yuan, H.; Jiang, P.; Guo, R.; Wang, L. High-Entropy Alloys as a Platform for Catalysis: Progress, Challenges, and Opportunities. *ACS Catal.* **2020**, *10* (19), 11280–11306.

(5) Wu, D.; Kusada, K.; Nanba, Y.; Koyama, M.; Yamamoto, T.; Toriyama, T.; Matsumura, S.; Seo, O.; Gueye, I.; Kim, J.; Rosantha Kumara, L. S.; Sakata, O.; Kawaguchi, S.; Kubota, Y.; Kitagawa, H. Noble-Metal High-Entropy-Alloy Nanoparticles: Atomic-Level Insight into the Electronic Structure. *J. Am. Chem. Soc.* **2022**, *144* (8), 3365–3369.

(6) Casado-Rivera, E.; Gál, Z.; Angelo, A. C. D.; Lind, C.; DiSalvo, F. J.; Abruña, H. D. Electrocatalytic Oxidation of Formic Acid at an Ordered Intermetallic PtBi Surface. *ChemPhysChem* **2003**, *4* (2), 193–199.

(7) Zhu, Z.; Liu, F.; Fan, J.; Li, Q.; Min, Y.; Xu, Q. C2 Alcohol Oxidation Boosted by Trimetallic PtPbBi Hexagonal Nanoplates. *ACS Appl. Mater. Interfaces* **2020**, *12* (47), 52731–52740.

(8) Luo, S.; Chen, W.; Cheng, Y.; Song, X.; Wu, Q.; Li, L.; Wu, X.; Wu, T.; Li, M.; Yang, Q.; Deng, K.; Quan, Z. Trimetallic Synergy in Intermetallic PtSnBi Nanoplates Boosts Formic Acid Oxidation. *Adv. Mater.* **2019**, *31* (40), 1903683.

(9) Wang, D.; Chen, Z.; Wu, Y.; Huang, Y.-C.; Tao, L.; Chen, J.; Dong, C.-L.; Veer Singh, C.; Wang, S.; Li Tao, C.; Key, S. Structurally Ordered High-Entropy Intermetallic Nanoparticles with Enhanced C–C Bond Cleavage for Ethanol Oxidation. *SmartMat* **2023**, *4* (1), e1117.

(10) Nakaya, Y.; Hayashida, E.; Asakura, H.; Takakusagi, S.; Yasumura, S.; Shimizu, K. I.; Furukawa, S. High-Entropy Intermetallics Serve Ultrastable Single-Atom Pt for Propane Dehydrogenation. *J. Am. Chem. Soc.* **2022**, *144* (35), 15944–15953.

(11) Peng, C.; Jia, Y.; Liang, J.; Xu, L.; Wang, G.; Mu, Y.; Sun, K.; Ma, P.; Prashanth, K. G. Electron Beam Melting of $(FeCoNi)_{86}Al_7Ti_7$ High-Entropy Alloy. *J Alloys Compd.* **2023**, 170752.

(12) Ma, J.; Xing, F.; Nakaya, Y.; Shimizu, K.; Furukawa, S. Nickel-Based High-Entropy Intermetallic as a Highly Active and Selective Catalyst for Acetylene Semihydrogenation. *Angew. Chemie Int. Ed.* **2022**, *61* (27), e202200889.

(13) Cui, M.; Yang, C.; Hwang, S.; Yang, M.; Overa, S.; Dong, Q.; Yao, Y.; Brozena, A. H.; Cullen, D. A.; Chi, M.; Blum, T. F.; Morris, D.; Finfrock, Z.; Wang, X.; Zhang, P.; Goncharov, V. G.; Guo, X.; Luo, J.; Mo, Y.; Jiao, F.; Hu, L. Multi-Principal Elemental Intermetallic Nanoparticles Synthesized via a Disorder-to-Order Transition. *Sci. Adv.* **2022**, *8* (4), 4322.

(14) Dey, G. R.; McCormick, C. R.; Soliman, S. S.; Darling, A. J.; Schaak, R. E. Chemical Insights into the Formation of Colloidal High Entropy Alloy Nanoparticles. *ACS Nano* **2023**, *17*, 5943–5955.

(15) Li, H.; Han, Y.; Zhao, H.; Qi, W.; Zhang, D.; Yu, Y.; Cai, W.; Li, S.; Lai, J.; Huang, B.; Wang, L. Fast Site-to-Site Electron Transfer of High-Entropy Alloy Nanocatalyst Driving Redox Electrocatalysis. *Nat. Commun.* **2020**, 11, 5437.

(16) Zhang, D.; Zhao, H.; Wu, X.; Deng, Y.; Wang, Z.; Han, Y.; Li, H.; Shi, Y.; Chen, X.; Li, S.; Lai, J.; Huang, B.; Wang, L.; Zhang, D.; Zhao, H.; Wu, X.; Deng, Y.; Wang, Z.; Han, Y.; Li, H.; Shi, Y.; Lai, J.; Wang, L.; Chen, X.; Li, S.; Huang, B. Multi-Site Electrocatalysts Boost PH-Universal Nitrogen Reduction by High-Entropy Alloys. *Adv. Funct. Mater.* **2021**, *31* (9), 2006939.

(17) Zhan, C.; Xu, Y.; Bu, L.; Zhu, H.; Feng, Y.; Yang, T.; Zhang, Y.; Yang, Z.; Huang, B.; Shao, Q.; Huang, X. Subnanometer High-Entropy Alloy Nanowires Enable Remarkable Hydrogen Oxidation Catalysis. *Nat. Commun.* **2021**, *12*, 6261.

(18) Wu, D.; Kusada, K.; Yamamoto, T.; Toriyama, T.; Matsumura, S.; Kawaguchi, S.; Kubota, Y.; Kitagawa, H. Platinum-Group-Metal High-Entropy-Alloy Nanoparticles. *J. Am. Chem. Soc.* **2020**, *142* (32), 13833–13838.

(19) Chen, Y.; Zhan, X.; Bueno, S. L. A.; Shafei, I. H.; Ashberry, H. M.; Chatterjee, K.; Xu, L.; Tang, Y.; Skrabalak, S. E. Synthesis of Monodisperse High Entropy Alloy Nanocatalysts from Core@shell Nanoparticles. *Nanoscale Horizons* **2021**, *6* (3), 231–237.

(20) Moreira Da Silva, C.; Amara, H.; Fossard, F.; Girard, A.; Loiseau, A.; Huc, V. Colloidal Synthesis of Nanoparticles: From Bimetallic to High Entropy Alloys. *Nanoscale* **2022**, *14* (27), 9832–9841.

(21) Broge, N. L. N.; Bondesgaard, M.; Søndergaard-Pedersen, F.; Roelsgaard, M.; Iversen, B. B. Autocatalytic Formation of High-Entropy Alloy Nanoparticles. *Angew. Chem., Int. Ed.* **2020**, *132* (49), 22104–22108.

(22) Sun, Y.; Zhang, W.; Zhang, Q.; Li, Y.; Gu, L.; Guo, S. A General Approach to High-Entropy Metallic Nanowire Electrocatalysts. *Matter* **2023**, *6*, 193–205.

(23)___Bueno, S. L. A.; Leonardi, A.; Kar, N.; Chatterjee, K.; Zhan, X.; Chen, C.; Wang, Z.; Engel, M.; Fung, V.; Skrabalak, S. E. Quinary, Senary, and Septenary High Entropy Alloy Nanoparticle Catalysts from Core@Shell Nanoparticles and the Significance of Intraparticle Heterogeneity. *ACS Nano* **2022**, *16*, 18873–18885.

(24) Zhang, D.; Shi, Y.; Zhao, H.; Qi, W.; Chen, X.; Zhan, T.; Li, S.; Yang, B.; Sun, M.; Lai, J.; Huang, B.; Wang, L. The Facile Oil-Phase Synthesis of a Multi-Site Synergistic High-Entropy Alloy to Promote the Alkaline Hydrogen Evolution Reaction. *J. Mater. Chem. A* **2021**, *9* (2), 889–893.

(25) Singh, M. P.; Srivastava, C. Synthesis and Electron Microscopy of High Entropy Alloy Nanoparticles. *Mater. Lett.* **2015**, *160*, 419–422.

(26) Fu, X.; Zhang, J.; Zhan, S.; Xia, F.; Wang, C.; Ma, D.; Yue, Q.; Wu, J.; Kang, Y. High-Entropy Alloy Nanosheets for Fine-Tuning Hydrogen Evolution. *ACS Catal.* **2022**, *12* (19), 11955–11959.

(27) Chen, W.; Luo, S.; Sun, M.; Wu, X.; Zhou, Y.; Liao, Y.; Tang, M.; Fan, X.; Huang, B.; Quan, Z.; Chen, W.; Luo, S.; Wu, X.; Zhou, Y.; Liao, Y.; Tang, M.; Fan, X.; Quan, Z.; Sun, M.; Huang, B. High-Entropy Intermetallic PtRhBiSnSb Nanoplates for Highly Efficient Alcohol Oxidation Electrocatalysis. *Adv. Mater.* **2022**, *34* (43), 2206276.

(28) Zhan, C.; Bu, L.; Sun, H.; Huang, X.; Zhu, Z.; Yang, T.; Ma, H.; Li, L.; Wang, Y.; Geng, H.; Wang, W.; Zhu, H.; Pao, C. W.; Shao, Q.; Yang, Z.; Liu, W.; Xie, Z.; Huang, X. Medium/High-Entropy Amalgamated Core/Shell Nanoplate Achieves Efficient Formic Acid Catalysis for Direct Formic Acid Fuel Cell. *Angew. Chem., Int. Ed.* **2023**, *62* (3), e202213783.

(29) Kim, H.; Yoo, T. Y.; Bootharaju, M. S.; Kim, J. H.; Chung, D. Y.; Hyeon, T. Noble Metal-Based Multimetallic Nanoparticles for Electrocatalytic Applications. *Adv. Sci.* **2022**, *9* (1), 2104054.

(30) Shelton, K. L.; Merewether, P. A.; Skinner, B. J. Phases and Phase Relations in the System Pd-Pt-Sn. *Can. Mineral.* **1981**, *19* (4), 599–605.

(31) Mayer, H. W.; Ellner, M.; Schubert, K. Kristallstruktur von Ir_5Sn_7. *J. Less-Common Met.* **1978**, *61* (2), P1–P7.

(32) Nowotny, H.; Schubert, K.; Dettinger, U. Zur Kenntnis Des Aufbaus Und Der Kristallchemie Einiger Edelmetallsysteme (Palladium-Blei, Palladium-Zinn, Iridium-Zinn, Rhodium-Zinn, Platin-Blei). *Int. J. Mater. Res.* **1946**, *37* (4–5), 137–145.

(33) Mourdikoudis, S.; Liz-Marzán, L. M. Oleylamine in Nanoparticle Synthesis. *Chem. Mater.* **2013**, *25* (9), 1465–1476.

(34) Mourdikoudis, S.; Menelaou, M.; Fiuza-Maneiro, N.; Zheng, G.; Wei, S.; Pérez-Juste, J.; Polavarapu, L.; Sofer, Z. Oleic Acid/Oleylamine Ligand Pair: A Versatile Combination in the Synthesis of Colloidal Nanoparticles. *Nanoscale Horiz.* **2022**, *7* (9), 941–1015.

(35) Sun, Y.; Terrones, M.; Schaak, R. E. Colloidal Nanostructures of Transition-Metal Dichalcogenides. *Acc. Chem. Res.* **2021**, *54* (6), 1517–1527.

(36) Ding, Y.; Zhang, N.; Zhang, J.; Wang, X.; Jin, J.; Zheng, X.; Fang, Y. The Additive-Free Electrode Based on the Layered MnO_2 Nanoflowers/Reduced, Graphene Oxide Film for High Performance Supercapacitor. *Ceram. Int.* **2017**, *43* (7), 5374–5381.

(37) Wang, G.; Liu, G.; Jin, Z. Interfacial Modification to Nanoflower-Like NiV-Layered Double Hydroxide for Enhancing Supercapacitor Performance. *ACS Appl. Nano Mater.* **2023**, *6* (10), 8603–8616.

(38) Page, K.; Schade, C. S.; Zhang, J.; Chupas, P. J.; Chapman, K. W.; Proffen, T.; Cheetham, A. K.; Seshadri, R. Preparation and Characterization of Pd_2Sn Nanoparticles. *Mater. Res. Bull.* **2007**, *42* (12), 1969–1975.

(39) Leonard, B. M.; Bhuvanesh, N. S. P.; Schaak, R. E. Low-Temperature Polyol Synthesis of $AuCuSn_2$ and $AuNiSn_2$: Using Solution Chemistry to Access Ternary Intermetallic Compounds as Nanocrystals. *J. Am. Chem. Soc.* **2005**, *127* (20), 7326–7327.

(40) Cable, R. E.; Schaak, R. E. Solution Synthesis of Nanocrystalline M-Zn (M = Pd, Au, Cu) Intermetallic Compounds via Chemical Conversion of Metal Nanoparticle Precursors. *Chem. Mater*. **2007**, *19* (16), 4098–4104.

(41) Leonard, B. M.; Schaak, R. E. Multistep Solution-Mediated Formation of $AuCuSn_2$: Mechanistic Insights for the Guided Design of Intermetallic Solid-State Materials and Complex Multimetal Nanocrystals. *J. Am. Chem. Soc.* **2006**, *128* (35), 11475–11482.

(42) Ma, T.; Wang, S.; Chen, M.; Maligal-Ganesh, R. V.; Wang, L. L.; Johnson, D. D.; Kramer, M. J.; Huang, W.; Zhou, L. Toward Phase and Catalysis Control: Tracking the Formation of Intermetallic Nanoparticles at Atomic Scale. *Chem* **2019**, *5* (5), 1235–1247.

(43) Guo, J.; Jiao, S.; Ya, X.; Zheng, H.; Wang, R.; Yu, J.; Wang, H.; Zhang, Z.; Liu, W.; He, C.; Fu, X. Intermetallic Nanocrystals: Seed-Mediated Synthesis and Applications in Electrocatalytic Reduction Reactions. *Eur. J. Chem.* **2022**, *28* (69), e202202221.

(44) Zhang, J.; Shao, Q.; Zhang, Y.; Bai, S.; Feng, Y.; Huang, X.; Zhang, J.; Shao, Q.; Zhang, Y.; Bai, S.; Feng, Y.; Huang, X. Promoting the Direct H_2O_2 Generation Catalysis by Using Hollow Pd–Sn Intermetallic Nanoparticles. *Small* **2018**, *14* (16), 1703990.

(45) Fu, L.; Zeng, X.; Huang, C.; Cai, P.; Cheng, G.; Luo, W. Ultrasmall Ir nanoparticles for efficient acidic electrochemical water splitting. *Inorg. Chem. Front.* **2018**, *5* (5), 1121–1125.

(46) Lacroix, L.-M.; Gatel, C.; Arenal, R.; Garcia, C.; Lachaize, S.; Blon, T.; Warot-Fonrose, B.; Snoeck, E.; Chaudret, B.; Viau, G. Tuning Complex Shapes in Platinum Nanoparticles: From Cubic Dendrites to Fivefold Stars. *Angew. Chem., Int. Ed.* **2012**, *51*, 4690– 4694.

Table of Contents Graphic